

Multiple failure styles related to shallow gas and fluid venting, upper slope Canadian Beaufort Sea, northern Canada



Francky Saint-Ange^{a,b,*}, Pim Kuus^{a,c}, Steve Blasco^a, David J.W. Piper^a, John Hughes Clarke^c, Kevin MacKillop^a

^a Geological Survey of Canada (Atlantic), Bedford Institute of Oceanography, P.O. Box 1006, Dartmouth, Nova Scotia B2Y 4A2, Canada

^b Department of Oceanography, Dalhousie University, Halifax, Nova Scotia B3H 4J1, Canada

^c Department of Geodesy and Geomatics Engineering, University of New Brunswick, P.O. Box 4400, Fredericton, NB E3B 5A3, Canada

ARTICLE INFO

Article history:

Received 7 August 2013

Received in revised form 27 April 2014

Accepted 24 May 2014

Available online 2 June 2014

Keywords:

gas seeps

creep

slope failure

permafrost

multibeam water column backscatter

Arctic

ABSTRACT

The continental slope of the Canadian Beaufort Sea presents an exceptional opportunity to study the relationship between the fluid venting and the formation of mass-transport deposits. The continental shelf was emergent and partially ice-free during the last glaciation and is underlain by widespread permafrost. Water-column backscatter has shown the locations of more than 40 active gas vents along seaward margin of the subsea permafrost at the shelf break and upper slope. New multibeam bathymetry and subbottom profiler data show shallow potentially late Holocene failures and mass-transport deposits on the upper slope. Upslope from a prominent headscarp, undulating seabed with apparent growth faults overlies an acoustically incoherent to stratified horizon at 50 m sub-bottom interpreted as a decollement surface over which progressive creep has occurred. Similar creep is present in places on the upper slope and in places seems to have evolved into small translational slides, involving more compacted sediment buried >25 m, or into muddy debris flows where sediments buried <25 m have failed. Much of the slope failed during a regional retrogressive event, the Ikit slump, likely initiated on steep channel walls on the lower slope. Characteristic ridge and trough morphology resulting from retrogressive spreading or rotational slumping are preserved on gradients <2° on the upper slope, but appear to have been completely evacuated on gradients of 3° on the mid slope, where muddy debris-flow deposits are found. Correlations between radiocarbon dated cores and sub-bottom profiles show that the retrogressive failure occurred in the last 1000 years. This study implies that Holocene shelf break and upper slope stability in the Beaufort Sea are strongly linked to the dynamics of the permafrost and the presence of weak, gas-rich sediments. It demonstrates that creep deformation evolves into either muddy debris flows or translational slides, dependent on sediment strength.

© 2014 Elsevier B.V. All rights reserved.

1. Introduction

Many authors regard earthquakes as the principal trigger of shallow slope failures, with increase in pore pressure by shallow gas as a preconditioning factor (Canals et al., 2004; Mosher et al., 2010). This topic has been the subject of hot debates during the past two decades over the key question as to what is the final trigger for submarine landslides (Canals et al., 2004). Where failure is widespread in multiple drainage systems, landslides are interpreted as triggered by earthquakes. In general, there is a lack of direct evidence for failures triggered by fluid circulation through sediment, although gas as the sole trigger cannot be entirely ruled out (Canals et al., 2004).

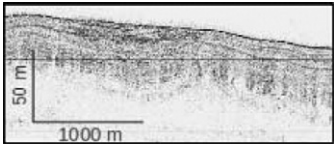
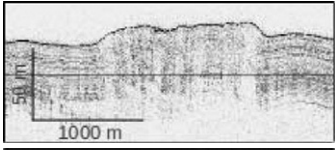
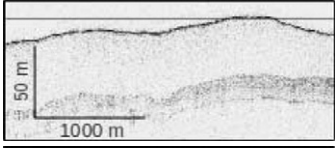
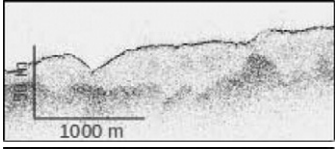
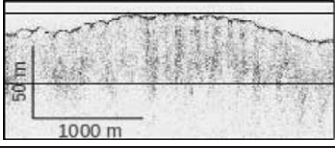
It has long been suggested that the presence of gas within shallow sediment could be the sole cause of certain slope failures (Sultan et al., 2004; Nixon and Grozic, 2007; Maslin et al., 2010; Li and He, 2012). Nevertheless positive feedback between fluid circulation and sediment

deformation leading to failure is poorly documented. Recent work has highlighted gas seep anomalies where slope failures have recently occurred (Faure et al., 2006; Rogers and Goodbred, 2010). The spatial or temporal relationship between gas seeps and slope failures has been recognised in several shallow water areas, such as the U.S. Atlantic margin, New Zealand, Norway and Bay of Bengal among others (Best et al., 2003; Hill et al., 2004; Faure et al., 2006; Panieri et al., 2012). In those cases sub-surface sediment deformation coupled with active gas escape structures have been identified and linked to different mechanisms, for instance wave pumping or soft sediment creep. In the case of sediment creep, it is suggested that the progressive deformation of a shallow water delta results from gas migration upslope leading to a modification of the sediment pore pressure related to sediment overloading (Hill et al., 2004). Creeping of sediment is a common process in deep water, and is not necessarily related to the presence of gas (Hill et al., 1982, 2004; Syvitski et al., 1987; Correggiari et al., 2001; Canals et al., 2004; Shillington et al., 2012). Creep is a slow but gradual elastic deformation of the sediment, which occurs over a relatively long period of time and can evolve into different sorts of slides

* Corresponding author.

E-mail address: fsaintange@gmail.com (F. Saint-Ange).

Table 1
Classification of 3.5 kHz acoustic facies.

| Type | Detail | Description | Occurrence |
|-------------|--------|---|---|
| Stratified | S1 |  | Undisturbed or remnant topography. |
| | S2 |  | Terminal of debris flow. |
| Transparent | T1 |  | Shelf, Slope, and mud volcano. |
| | T2 |  | Beyond slumps |
| Chaotic | C |  | Slumps from escarpments to gentle topography down slope and channels. |

or into plastic to liquefied mass flow (Mulder and Cochonat, 1996). Creep does not necessarily lead to failure but causes permanent deformation to the sediment, although creep is characteristic of areas predisposed to failures. As for other classic failures, earthquakes can affect the creep in accelerating the process leading to the failure. Most of the documented examples of sediment creep in deep water involve muddy sediment deposited over a detachment layer (Correggiari et al., 2001; Shillington et al., 2012) and in some cases the detachment layer could be related to the presence of gas within a sandy unit overlaid by a thick clay rich unit (Hill et al., 2004). In such a case, the evolution from creep to failure relies on a positive feedback between the gas charge in the sandy layer and the load of the muddy unit. Yet, the interplay between gas and sediment in areas prone to failures is still not well documented.

In this study, we examine the upper slope seaward of the central Beaufort Shelf (Fig. 1), in the Arctic Ocean, where venting of fluids including gas is concentrated. The objectives of this study are: (1) to document the regional distribution of gas venting; (2) to characterise the style of recent sea-bed failure on the upper slope; and (3) to evaluate the role of shallow gas in the initiation and deformation of the mass-transport deposits.

2. Geological setting

The Mackenzie Delta occupies the central portion of the late Mesozoic to Cenozoic Beaufort-Mackenzie structural basin and today discharges onto a 100 km wide continental shelf in the Beaufort Sea. During the last glacial maximum, the continental ice sheet crossed the shelf to present day shelf edge for short time periods and left the shelf emergent for long periods (Blasco et al., 2013). Retreat of the ice front from the shelf edge resulted in the deposition of glaciomarine sediments, which pinch out at the shelf edge but thicken down slope. Although the Mackenzie River has the largest sediment load of any river discharging into the Arctic Ocean, $\sim 127 \times 10^6 \text{ Mt} \cdot \text{a}^{-1}$ (Carson et al., 1998), little sediment finds its way to the central shelf edge as

the Coriolis force drives the sediment plume east along the inner shelf (Vilks et al., 1979; Blasco et al., 2012).

On the Beaufort Shelf, the top 100 m of sediment is no older than $\sim 27 \text{ ka}$ (Hill et al., 1985) and represent late Wisconsinan to Holocene deposition that continues down slope (Blasco et al., 2013). Sedimentation rates of $\sim 1.4 \text{ m} \cdot \text{ka}^{-1}$ have been estimated for the uppermost Beaufort Slope in the late Holocene, highlighting the significant contribution of the Mackenzie River to the slope following deglaciation (Scott et al., 2009; Bringué and Rochon, 2012). A core at 671 m in the Mackenzie Trough shows 8 m of soft mid- to late Holocene silty muds overlying well laminated early Holocene to late Pleistocene muds (Schell et al., 2008). At 1000 m on the Beaufort Slope, the mid- to late Holocene silty muds are only 2 m thick and overlie rather uniform clays with thin sandy intervals (Scott et al., 2009).

Earthquake activity is quite low in the Canadian Beaufort region and is mostly related to the crustal response of a large uncompensated sediment load along the continental slope (Atkinson and Charlwood, 1988). Seismicity is usually of a low magnitude (<4) but a few events with magnitude greater than 5 have been reported in the 100 years of instrumental records (Lamontagne et al., 2008; Cassidy et al., 2010).

The Beaufort Shelf contains more than 700 m of ice-bearing sediments (Blasco et al., 2013). These frozen sediments pinch out at $\sim 100 \text{ m}$ water depth, coincident with the current shelf edge. The impermeable ice-bearing sediments form a barrier to migrating fluids. Over geologic time these fluids have migrated to the northern edge of the permafrost and escape to the seabed in the area of the shelf break. Concentrated fluid escaping at the permafrost edge has resulted in the formation of a linear array of over 700 mud volcanoes along the current shelf edge (Blasco et al., 2013).

3. Methods

Acoustic data were collected in 2009 and consisted of Kongsberg-Simrad 30 kHz EM302 multibeam sonar and Knudsen 3.5 kHz sub-

bottom profiler. In order to insure 100% bottom coverage of bathymetry, survey-lines were oriented along the slope at 1000 or 250 m interval depending on water depth. The EM302 was operated in dual-swath mode which employs a second swath that is transmitted before the previous swath is received. This new option allows increased along track resolution. Each swath is made up of 288 1.0×1.0 degree beams but yields 432 soundings by deriving multiple solutions through phase differences in the time series of oblique beams (high density mode). The EM302 also collects seabed and water column backscatter data in addition to bathymetry. Bubble-wash-down due to increasing sea state degraded the seabed backscatter quality on some survey lines, although the bathymetry was not affected.

All multibeam and sub-bottom data were processed using UNB/OMG SwathEd processing software (Hughes Clarke, 2012). Soundings were gridded, factoring in the beam widths, and a weighting function was used favouring near-nadir beams at overlap. Seabed backscatter beam pattern artefacts were reduced using empirically derived beam-pattern correction models for each survey line (similar to Hughes Clarke et al., 2008). Backscatter data were corrected for grazing angle effects based on the local bathymetry. The digital terrain model and backscatter mosaic were gridded at 15 m resolution (Figs. 1 and 2). Globally corrected C-Nav dGPS solutions were applied to all data and soundings were reduced to mean sea level using the tidal model WebTide.

Past studies using multibeam water column data highlighted the potential to visualize features in 3-dimensions such as aquatic vegetation, shipwrecks, oceanographic features, turbidity currents and of particular interest to this study, plumes of venting gas in the water column (Schneider von Deimling et al., 2007; Hughes Clarke et al., 2012). Water column backscatter is a novel feature that images the scatters within the minimum slant range to the seabed (e.g. Hughes Clarke, 2006). Data outside the minimum slant range would be heavily

contaminated due to side-lobe echoes from oblique beams. The effective water column is therefore reduced to a half cylinder space from the transducer to nadir. Return intensities of all receiver beam-forming channels (288 in total for the EM302) are logged. Due to a larger acoustic impedance contrast at the bubble interface, stronger backscatter levels are observed where gas bubbles are present. As a result of the dense beam spacing (particularly near the transducer), a cross section of the plumes are collected as the ship transverses over each active gas vent and is subsequently mapped in 3D.

4. Results

4.1. Morphology

4.1.1. Regional morphology

The Beaufort Shelf consists of a series of banks (termed plateaus or plains) separated by transverse troughs or channels (Blasco et al., 2013). Present multibeam coverage extends over a $\sim 120 \times 50$ km area on the upper Beaufort slope (Fig. 1), seaward of the Kugmalit Channel, Akpak Plateau, Ikit Trough and the eastern part of the Kringalik Plateau. Water depths range from ~ 70 m on the outer shelf to 1500 m on canyon floors. The shelf break is located at ~ 120 m water depth. The slope of the shelf break is gentle over a progradational feature at the seaward end of Ikit Trough, here termed the Ikit Delta, and seaward of the Akpak Plateau ($<2^\circ$) and becomes steeper to the southwest seaward of the Kringalik Plateau ($>5^\circ$) (Fig. 2). Near the shelf break are contour-parallel ridges and conical mounds (Fig. 2), locally referred to as pingo-like-features (PLFs) because they were originally interpreted as the seabed equivalent of ice-cored pingos mapped on the Tuktoyaktuk peninsula (Shearer et al., 1971), but are now regarded as mainly mud volcanoes (Blasco et al., 2013). Beyond the shelf break to ~ 1000 m, slopes are gentle ($<2^\circ$). Two deeply incised slope canyons, orientated

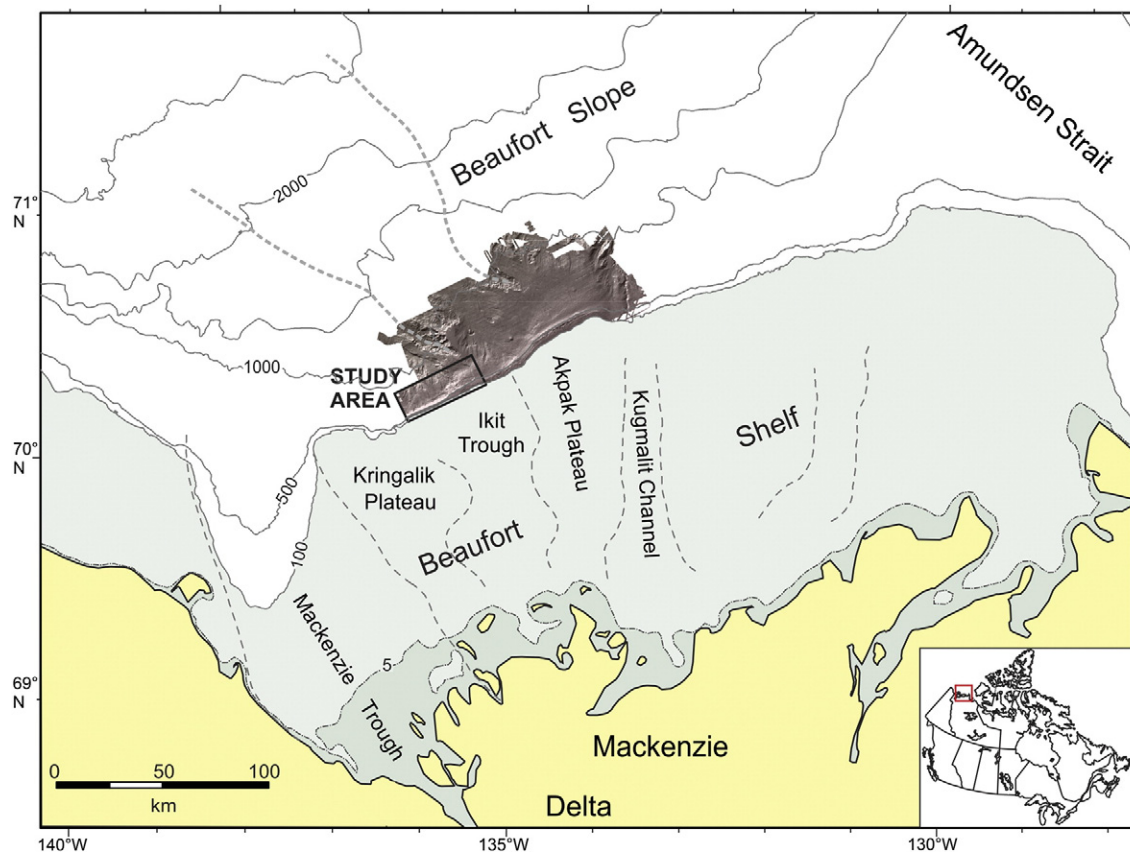


Fig. 1. Map showing location of the study area on the upper Beaufort Slope and the distribution of CCGS Amundsen EM302 multibeam bathymetry collected between 2009 and 2010.

in north-westerly direction, start at ~600 m and the canyon floors have been mapped to 1500 m water depth (Fig. 1). Three large mud volcanoes are observed at deeper water depths on the slope, each with a planar top measuring between 500 and 1000 m in diameter and 10 to 30 m high (e.g., MV, Fig. 2). Several hundred smaller sized conical mounds occur in a linear array along the shelf edge (Blasco et al., 2013). Relict ice scours generated by the passage of drifting iceberg keels from ablating glacial ice are observed on the slopes from the shelf break to 600 m (e.g. Sc in Fig. 2).

4.1.2. Morphology of the study area

The study area is in the southwest portion of the multibeam block and measures 40×14.5 km (Fig. 2). The shelf is mostly featureless, except for some sea-ice ice-keel scours and PLFs concentrated in the northern part of the area (Fig. 2). PLFs are typically grouped parallel to the shelf edge, although their presence is not as numerous as in neighbouring areas northeast of the study area (Fig. 1). The shelf edge is identified at approximately the 120 m isobath and corresponds to the seaward limit of sub-sea acoustic permafrost described by Blasco et al. (2013).

The continental slope in the study area extends to the 750 m isobath and shows complex topography. Much of the seabed shows chaotic topography (CT in Fig. 2) of the type commonly associated with mass-transport deposits (MTDs) in the literature (Mosher et al., 2010). Other parts of the slope show smooth topography (ST) extending downslope from the shelf edge. Small isolated areas of smooth topography surrounded by lower chaotic topography are identified as remnant undisturbed topography (RT in Fig. 2). Other smaller features include channels (Ch) and escarpments (Es) that bound chaotic topography and mud volcanoes (MV in Fig. 2).

The north-eastern section of the study area has gentle slopes from the shelf (~2°) down to ~670 m water depth. A large mud volcano is observed at ~300 m water depth (Fig. 2). This planar-topped mound sits at ~10 m above the seabed surrounded by a pronounced moat. Backscatter quality in this part of the margin is poor, though sufficient to confidently determine little backscatter change in the area aside from the mud volcano, which stands out with strong backscatter levels (Fig. 3).

The central and south-western parts of the study area show steep slopes at the shelf break with slopes changing from <2° to 5–19°. The central part is characterised by a chaotic topography corresponding to a set of slope failure deposits which appear to have originated from near the shelf break and collectively form the Ikit slump (Fig. 2). Curvilinear sub-parallel blocks, commonly with concave downslope crests, are observed in the upper part of the deposit with average size around 2 m high and 150 m wide. Based on the backscatter intensity and the bathymetric data, this area of chaotic topography can be subdivided in four distinct zones, identified as Z1 to Z4 in Figs. 2 and 3. Zones 1, 3 and 4 show similar characteristics (Fig. 2). Channels appear to be almost nonexistent or quite indistinct. A disconnected section of remnant topography is found between zones 3 and 4. The backscatter levels are weak, with weaker levels for zone 3 then zone 1 (Fig. 3). The chaotic topography shows a pattern of discontinuous curvilinear ridges with a typical spacing of 150–200 m and heights of 200 m. The ridges are clearest up slope and become increasingly muted downslope below the 300 m isobath.

Zone 2 shows highly eroded morphology, unlike zones 1, 3 and 4. The axial part shows a dense network of merging channels feeding the canyons downslope (Figs. 2, 3), with some upper slope remnant topography. This zone is unique in backscatter level and is characterised by strong amplitude in signal strength from the PLFs down to the limit of

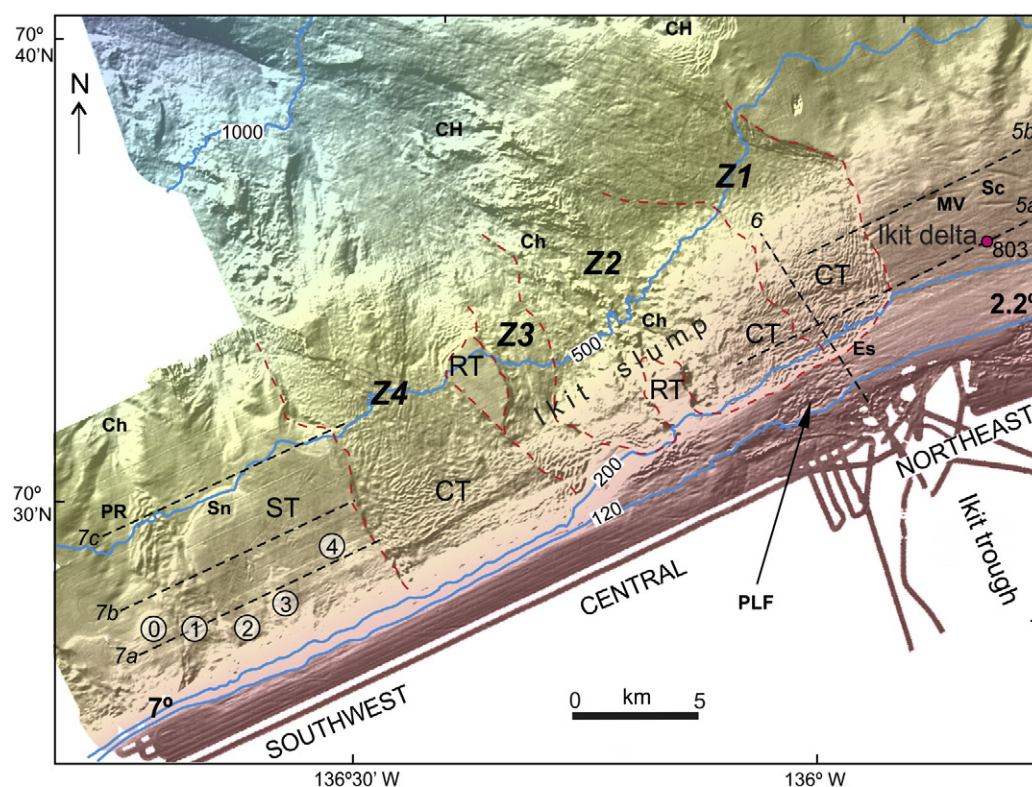


Fig. 2. Bathymetry of the study area. Major morphological zones Z1 to Z4 are outlined by red dashed lines: CT = chaotic topography, RT = remnant topography; ST = smooth topography. Features include canyon heads (CH), channels (Ch), escarpments (Es), mud volcanoes (MV), parallel ridges (PR), pingo-like features (PLFs), and scours (Sc). Dashed lines show location of profiles in Figs. 5, 6 and 7. (0) to (4) are MTDs identified in Fig. 7 and in text.

data coverage, with sub-parallel fingers of weaker and stronger signal strength corresponding to numerous shallow channels (Fig. 3).

In the south-western part of the study area, smooth topography is observed from the shelf break to ~550 m water depth (Fig. 2). In detail, the bathymetric data show various lobes extending downslope. One particular lobe extends beyond the smooth topography and shows several consecutive sub-parallel transverse ridges (PR in Fig. 2), with crest convex downslope. Immediately east of this, a prominent lobate feature appears to have a curved ridge parallel and downslope of its termination. All these lobe-like bodies appear to originate from the shelf break, which is a very linear feature. Uniformly weak backscatter levels are observed (Fig. 3).

4.2. Surficial geology

4.2.1. Sub-bottom echo-facies

Based on sub-bottom profiler data, three main types of echo-facies were defined for the study area: transparent (T), stratified (S) and chaotic (C) (Fig. 4). Stratified and transparent facies are subdivided in two sub-groups based on specific characteristics (Fig. 4). Using this classification and dense survey line spacing, the acoustic types within the study area have been delineated. All three types of echo-facies overlie a deeper incoherent unit characterised by a transparent echo-facies ("deformed unit" in Fig. 5).

The chaotic echo-facies are characterised by dense irregular small hyperbolae at the seabed (Fig. 6) and in places a basal reflector. Chaotic seafloor influences the backscatter character (compare Z1 with the stratified Ikit Delta in Fig. 3). The transparent echo-facies is characterised by lack of internal reflectors and thin or prolonged surface echo with the presence of a basal reflector (T1), or a discontinuous and faint basal reflector (T2) (Figs. 4, 7 and 8). Stratified echo-facies correspond to parallel and continuous reflectors, which may be distinct with continuous subsurface reflectors (S1) or slightly disturbed with discontinuous subsurface reflectors (S2).

4.2.2. Facies distribution and related deposits

On the slope, the stratified echo-facies (S) is found in the smooth topography of the Ikit Delta in the north-eastern area and below 500 m water depth in the south-western area (Fig. 7). Transparent (T) units are found in the central area with chaotic topography and in the south-western area of smooth topography (Figs. 5 and 7). Chaotic (C) facies correspond to the chaotic topography on the slope (Figs. 2, 5 and 7) and gradually changes into T2 facies downslope (Fig. 7). The shelf is mostly of type T1, including the areas around the PLFs, and stratified sediments are found only locally (Fig. 5).

The stratified echo-facies is found in the undeformed part of Ikit Delta, which shows prograding stratified sediment, the upper part of which is shown in Fig. 6. The stratified sediment is ~75 m thick at the shelf break and decreases to ~40 m downslope. The stratified sediment overlies a more transparent unit showing varying degrees of internal deformation described below (Fig. 5). Echo-facies S2 is present along much of the uppermost slope below the 120 m isobath down to 150–200 m (Fig. 4). It is also present in a few small areas where some remnant topography is more or less preserved within the chaotic topography of the slope.

In deeper water in the southwest area, echo-facies S2 (Fig. 7b, c) corresponds to the parallel ridges in surface morphology (PR in Fig. 2). The facies is cut by subvertical faults (Fig. 7b) and appears to have an overthrust contact with stratified facies S1 to the southwest.

More generally, in echo-facies S2, and less prominently also in S1, the stratified sediment is cut by faults and tension cracks and may appear folded (e.g., (a) in Fig. 5a; S2 in Fig. 7c). The faults are most clearly shown in low vertical exaggeration zooms in Figs. 5a and 6d. Many of these faults appear to be growth faults, in which deformation increases with sub-bottom depth (e.g., (a) in Fig. 5a). Furthermore, at some sub-surface horizons, buried depressions, possibly pockmarks, overlie deeper sub-vertical features that resemble fluid chimneys (e.g. (b) in Fig. 5a, (c) in Fig. 5b).

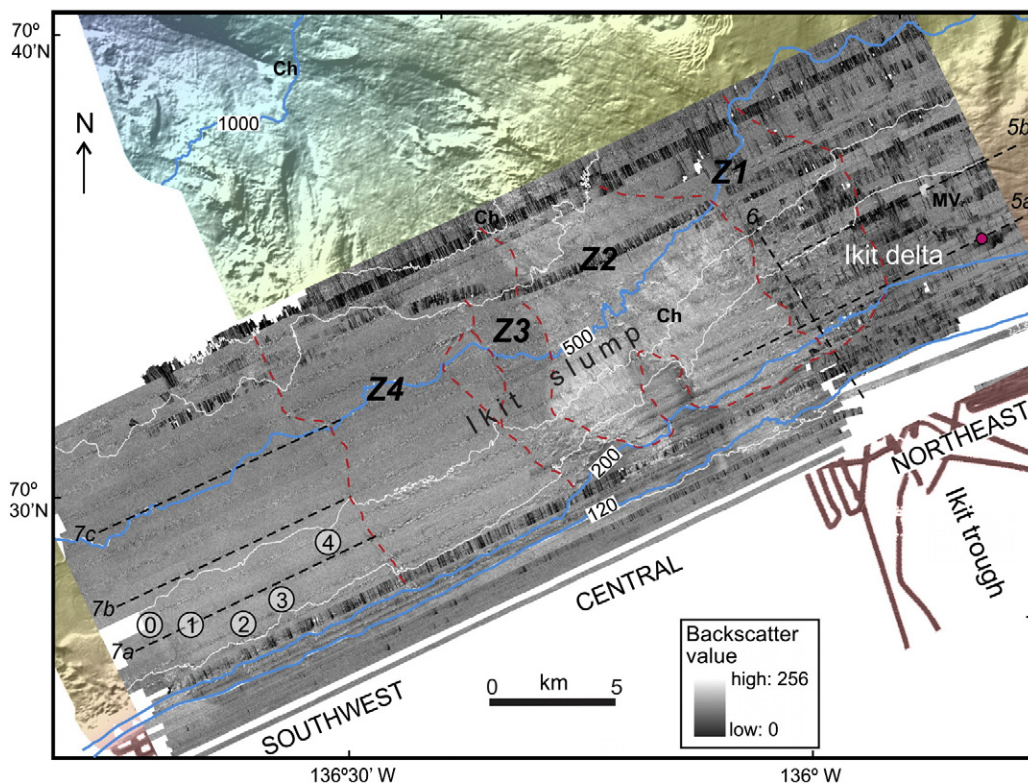


Fig. 3. Acoustic backscatter data for the study area. Abbreviations as in Fig. 2.

Transparent echo-facies are well developed in the south-western area (Fig. 7). A 25–50 m thick sheet of facies T1, becoming less extensive downslope, overlies a prominent reflector package of facies S1 (north-eastern part of Fig. 7a–c). In Fig. 7c, this sheet shows a steep lateral contact with S1 stratified sediment, but the upper ~2 m of the stratified section appears continuous with the T1 unit. Based on reflection amplitude of the underlying horizon, the T1 body is as acoustically transparent as the laterally equivalent S1 section. The T1 sheet shows a possible lateral facies change into deformed stratified sediment S2 to the southwest (Fig. 7b). Part of unit T1 overlying a small ridge in the underlying strata has patchy higher acoustic reflectivity and there are bright spots in the underlying stratified sediment (Fig. 7b). Another smaller high-reflective T1 facies has a small PLF with a central crater at the seabed (Fig. 7b).

Chaotic echo-facies correspond to the chaotic topography on the slope (Figs. 2, 5 and 7) and gradually changes into T2 transparent facies downslope (Fig. 6). Upslope, this transparent facies in places appears to overlie buried chaotic facies, but downslope appears to overlie a strong subsurface reflection (Fig. 6, northwest end). The chaotic facies in zone 4 extends down to 550 m water depth, whereas it extends only to 300–350 m in zones 1 and 2 (Fig. 2). The observed thickness of the chaotic facies in the area of chaotic topography ranges from >75 m upslope to less than 50 m downslope (Fig. 6). The deposits also thin laterally and fill pre-existing channels. In some dip sub-bottom profiles, the chaotic facies can be seen to consist of discrete blocks, 150–300 m wide, that dip upslope (Fig. 6). Patchy bright spots (Fig. 6) may indicate the presence of free gas. No relative age can be inferred from sub-bottom profiles in zones 1 to 4.

A distinctive *deformed unit* (D) underlies a 20–40 m thick unit of facies S1 on the outer shelf and upper slope. It continues beneath the unfailed smooth slopes of the north-eastern part of the Ikit Delta (Figs. 5, 8), where the deformed unit is similar to that on the outer shelf and uppermost slope and is demonstrably linked to gas at the

mud volcano (Fig. 5b). In the adjacent zone of chaotic topography to the west, transparent facies appear to overlie the continuation of the top of the deformed unit distally (lines 1 and 2, Fig. 8) or overlie a deeper horizon within or below the deformed unit (lines 3–6, Fig. 8).

In places the deformed unit has a transitional contact with the overlying S1 facies (Fig. 5a), in other places it appears abrupt, either conformable (Fig. 5b) or disconformable ((d) in Fig. 5a). Much of the unit appears acoustically incoherent, in part because of insufficient energy return. The association with gas venting (Fig. 5b) suggests that there may be some gas blanking. Some remnants of stratified facies show patchy high amplitude reflections or “bright spots”. Other remnants of stratified facies appear folded (Fig. 8).

4.3. Multibeam water column backscatter (MWCBC)

Gas plumes were imaged in three dimensions in multibeam water column backscatter data (Figs 9, 10). Narrow sinuous plumes, either solitary or grouped, are observed escaping from the seabed (Fig. 9). In the study area, only one active gas vent on the slope was associated with a PLF (Fig. 5b). The vents at the shelf edge are most common in a zone between the 90 and 200 m isobaths (Fig. 4). Gas plumes are between 30 and 40 m high and disappeared near 40 m water depth (Fig. 9). Of significance, none of the water column plumes were associated with mud volcanoes or PLFs but occurred in association with facies contacts or at the crest of headwall escarpments of slumps.

The gas vents near the shelf edge occur in four clusters (Fig. 4). Cluster A corresponds to the vents found near the headwall escarpment upslope from the chaotic topography west of the Ikit Delta. All are between the 150 m and 210 m isobaths. Cluster B (11 vents) is located near the boundary between chaotic and smooth topography in water depths of <100 m. Ten vents have solitary plumes and one has multiple plumes. Cluster C comprises only two vents, both with multiple plumes, on the outer shelf in the central part of the study area. Cluster

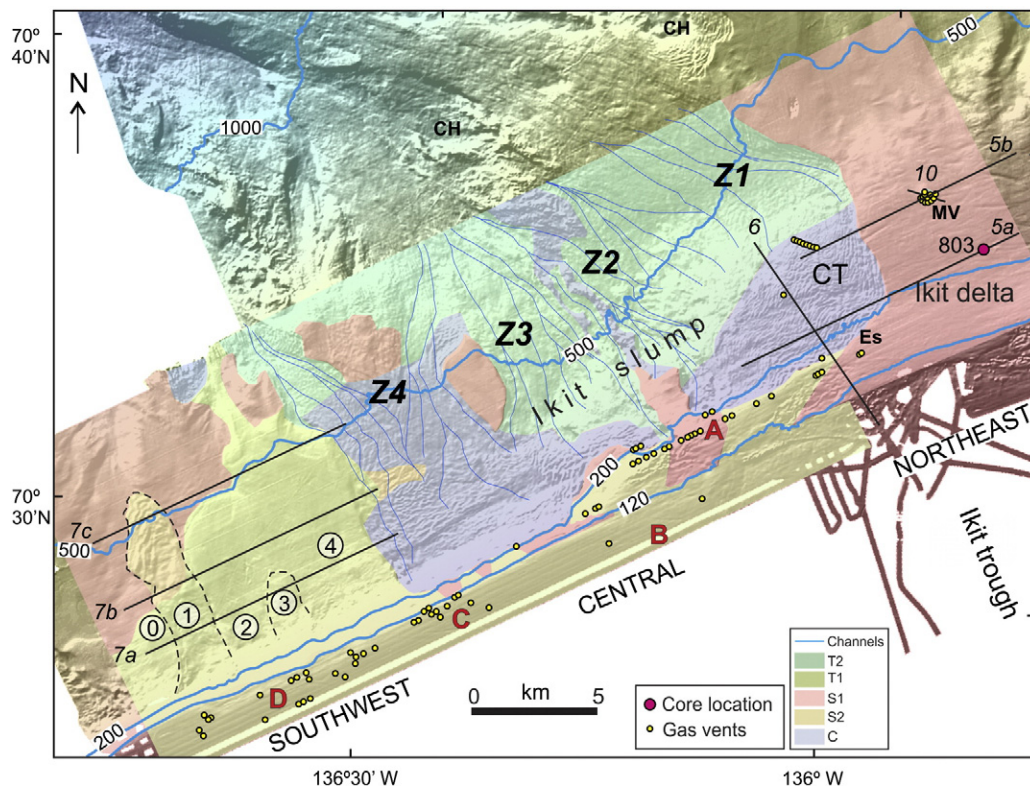


Fig. 4. Surficial acoustic facies map based on the classification in Table 1. Also shows the distribution of active gas vents recognised from EM302 multibeam water column backscatter. Lines show location of illustrated sub-bottom profiles.

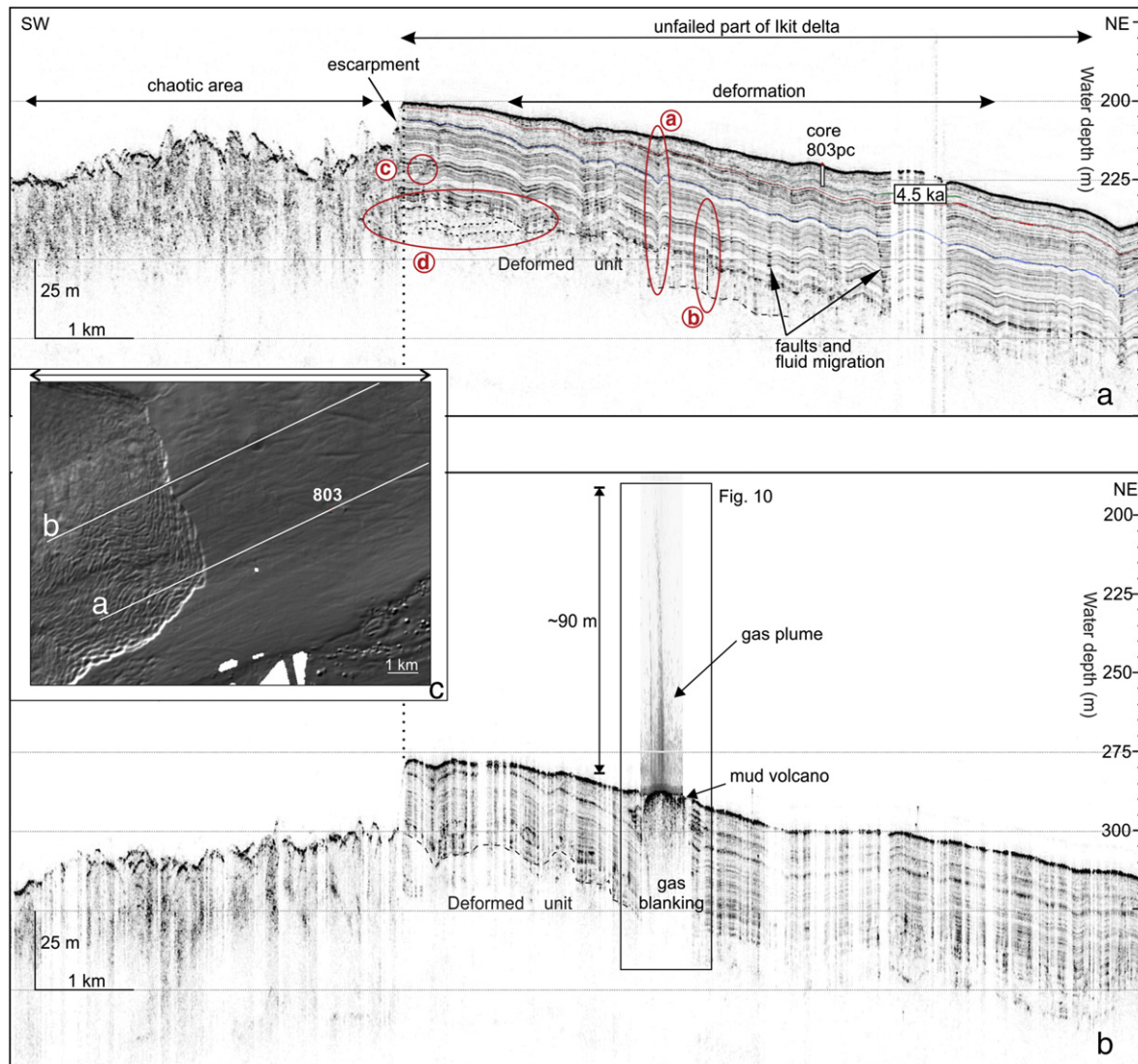


Fig. 5. Slope-parallel sub-bottom profiles across the Ikit Delta from chaotic slump to stratified undisturbed seabed, (a) near the 220 m isobath and (b) near the 290 m isobath. (c) shows the corresponding multibeam bathymetry. Profile (a) also show location of core 803 PC (Bringué and Rochon, 2012), reflector chronology inferred from radiocarbon dates in that core, and deformation features: (a) and (b) are growth faults diminishing in throw upwards, (c) is a buried pockmark and (d) shows disconformable relationships at the top of the deformed unit.

D is located upslope from the smooth topography overlying MTDs in the south-west of the study area. It consists of 22 vents, mostly with solitary plumes, all shallower than the 100 m isobath.

On the continental slope, gas venting activity was found at the large mud volcano (Fig. 10) and a few other vents are located within the chaotic facies (Fig. 5). Because the water column data is optimized near nadir, it appears as if most plumes were situated in a linear fashion along the ship's track. However, they are more likely dispersed. Seven significant gas plumes were observed at the centre of the large mud volcano and in the moat. The largest gas plume is approximately 90 m high and rises up to 100 m water depth (Fig. 10).

5. Discussion

5.1. The presence of subsurface gas

The abundance of gas plumes observed on multibeam water column backscatter data and bright spots on sub-bottom profiles (Figs. 5 and 7) indicates that gas is abundant in sub-surface sediment, as noted elsewhere on the Beaufort Shelf (Paull et al., 2007) and slope (Paull et al., 2012). The greatest abundance of active vents is near the seaward

limit of sub-sea permafrost (Fig. 4), indicating that the permafrost influences the escape of fluids from shelf sediments (Paull et al., 2012). Regionally, the sub-bottom profiler data show a prominent, deformed sub-surface layer (D) beneath the upper slope and outer shelf (Fig. 5a) that, where connected to the surface through pingo-like features (Fig. 5b), is directly associated with gas venting. This deformed unit shows patchy lateral variation in reflection amplitude, a feature commonly associated with subsurface gas (Casas et al., 2003). The presence of subsurface gas is also confirmed through the observation of gas plumes within the major slump and at the headwall escarpment of the MTDs observed in the southwest part of the study area (Fig. 4).

5.2. Creep on the outer shelf and upper slope

The undulating character of the T1 facies on the uppermost slope was identified as resulting from creep more than 30 years ago by Hill et al. (1982). Subsequently, however, it was realised that similar structures might result from plume fall-out draping a blocky MTD (e.g. Mosher et al., 2010). Apparent faults in a creep block might be seismic artefacts, as in the controversy over the "Humboldt Slide", where a rotational slump was later interpreted as depositional sediment

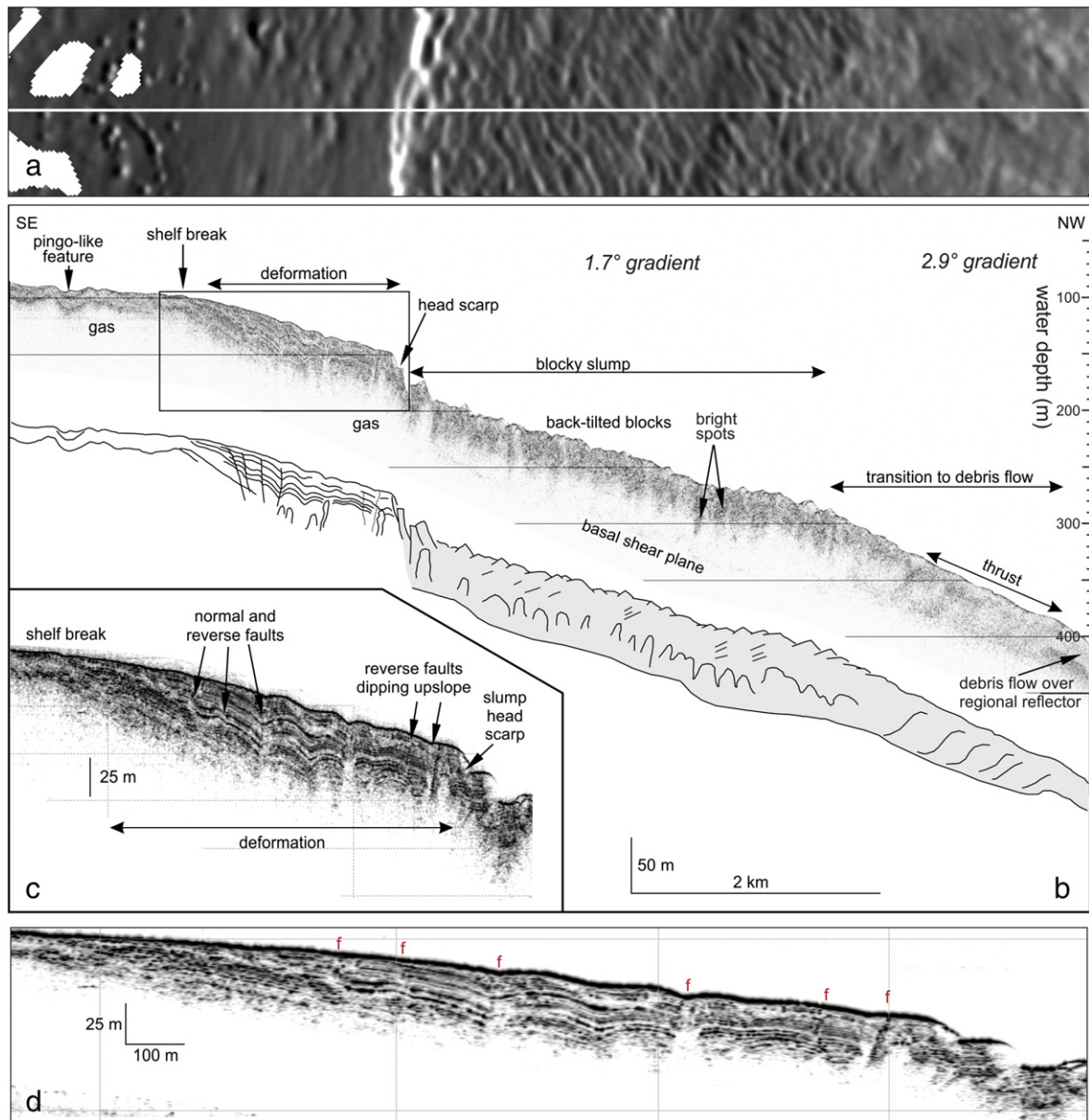


Fig. 6. (a) Downslope sub-bottom profile (above) off the Ikit Delta and derived sketch (below) illustrating transparent, stratified, and chaotic sub-bottom facies. (b) Detail of profile at shelf break. (c) Corresponding multibeam bathymetry. See Figs. 2 and 4 for location.

waves (Lee et al., 2002; Urgeles et al., 2011). This paper provides additional justification for a creep origin for T1 facies undulations that was not available to Hill et al. (1982).

The stratified sediments (S1) over the acoustically incoherent deformed layer (D) are cut by subvertical mud diapirs on a variety of scales (d in Fig. 8), the largest forming a clear volcano at the seabed (Fig. 5b). In places, subvertical growth faults are imaged (a in Fig. 5a; g in Fig. 8) in profiles slightly oblique to strike but many of these faults dip upslope in dip lines (Fig. 6b), in a manner suggesting local compression. In places, probable tension cracks are interpreted (t in Fig. 8): they show no offset of strata, but have enhanced reflectivity perhaps due to fluids. The rapid thickness changes and irregular top surface of the deformed layer might be a blocky MTD, but the setting is unusual on the outer shelf. The mud volcanoes indicate high mobility of sediment from the deformed layer rather than the layer consisting of large indurated blocks. It is possible that some of the wavy morphology is related to sediment transport processes, as argued elsewhere by Urgeles et al. (2011). However, the amplitude

of the wave-like forms decreases upwards from the underlying deformed layer to the seabed (Figs. 5a, 6c) and fault offsets of strata are visible in the “troughs”, with the greatest offset at depth (e.g. (b) in Fig. 5a). For these reasons, we interpret the wave-like features as principally deformational. The underlying deformed layer thus appears to be a gassy decollement surface of weak and deformed sediment over which the surficial 20–40 m of stratified sediment is creeping. The observed growth faults and tension cracks indicate that this creep has been progressive over the time span of deposition of most of the stratified unit.

Core 803 PC of Bringué and Rochon (2012) penetrates the upper 6 m of the stratified unit (Fig. 5a). The core consists of silty clay with a variable degree of bioturbation. No sedimentary structures such as ripples or turbidite laminae related to gravity currents were observed, therefore supporting the hypothesis that the wavy pattern of the seabed does not correspond to sediment waves. The core yielded an age of 4.5 ka at its base, giving a sedimentation rate of about $1.27 \text{ m} \cdot \text{ka}^{-1}$. Sedimentation rates may have been higher in the early Holocene and late Pleistocene,

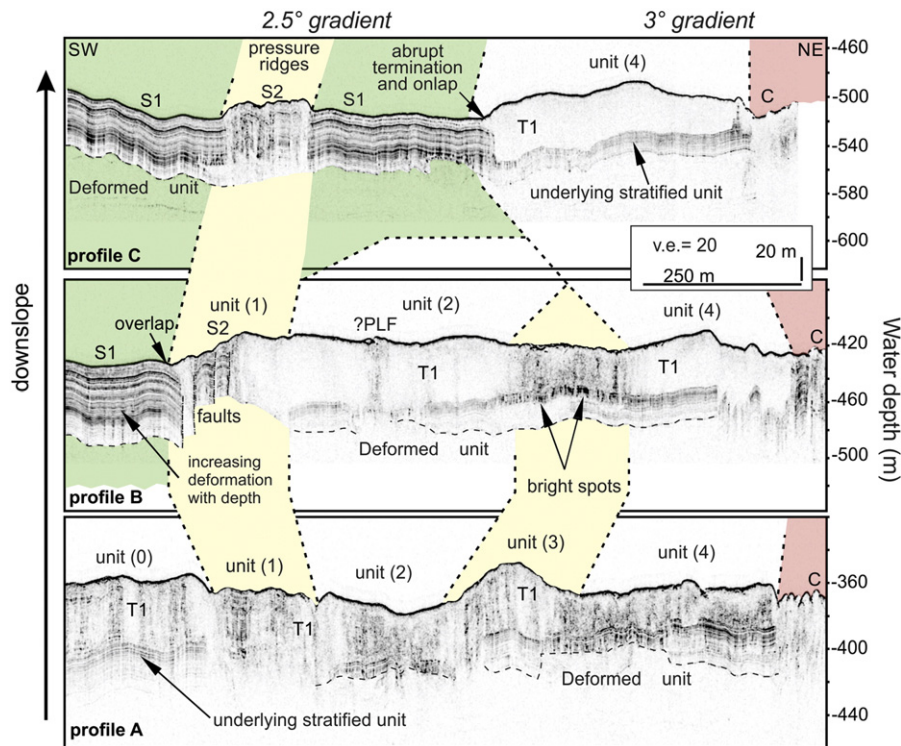


Fig. 7. Consecutive sub-bottom profiles crossing the smooth topography on the southwestern slope showing the downslope evolution of several MTD units. See Figs. 2 and 4 for location and text for details.

but this core suggests that creep has been active for many thousands of years.

5.3. Rotational slumping or spreading in the central area

5.3.1. Failure of the Ikit slump on the western Ikit Delta

The chaotic topography north of the upper slope headscarp in zones 1, 3 and 4 southwest of the Ikit Delta (Fig. 2) shows a pattern of discontinuous curvilinear ridges that become increasingly muted downslope below the 300 m isobath. This pattern is very similar to that produced by rotational retrogressive slumps at the sea-floor, rotating on a basal weak layer, that downslope are progressively overlain by debris-flow deposits formed by the break-up of the slumped blocks, well documented in the failure area of the classic 1929 Grand Banks failure (Piper et al., 1999). Similar ridges are present in the upper part of the Storegga Slide, where Micallef et al. (2007) interpreted them to result from spreading translation over a deforming mass of underlying material. Which of these two processes was active in the Ikit slump is unclear from the available data. Both failure types can occur in a retrogressive manner. Such a retrogressive failure may have been initiated on steep channel walls such as those north of the study area between 700 and 1000 m water depth and propagated upslope to the shelf edge.

It cannot be determined with our data whether failure took place in one or more episodes. However, the morphological continuity of ridge patterns in zone 1 from the headwall scarp to the 400 m isobath suggests that part of the failure represents a single event. Rotational failure or spreading took place on a weak zone coincident with the deformed unit beneath the unfailed smooth slopes of the north-eastern part of the Ikit Delta (Fig. 8). The water column backscatter data clearly shows the gas plumes along the headwall escarpment and within the upper part of the slump, which is in a good agreement with a failure related to gas-rich sediment (Kvenvolden, 1999; Rogers and Goodbred, 2010).

The lack of detectable sediment cover on the blocks of the zone 1 slump and the outcropping on the headwall scarp of shallow reflections

(Fig. 5a) dated in piston core 803 PC and box core 803BC (Bringué and Rochon, 2012) indicates that the failure is young, probably in the last thousand years, given that the late Holocene sedimentation rate in this area is $\sim 1.4 \text{ m} \cdot \text{ka}^{-1}$ (Scott et al., 2009; Bringué and Rochon, 2012). The slump may have been triggered in a distal location where free gas was less abundant but slopes were steeper, then retrogressed on the gas-charged weak decollement zone that extends beneath the creep folds in stratified facies.

5.3.2. The backscatter character of the Ikit slump

The Ikit slump is characterised by lateral changes in the backscatter data that do not correspond to lateral changes in the 3.5 kHz data (Figs. 3 and 8). Similarly, the 3.5 kHz data show a downslope evolution from chaotic to incoherent unit that does not correspond to significant changes at the seabed in the backscatter signal strength (Fig. 8). The transition from weak to high backscatter level does correlate to the lateral thinning of the slump deposits that filled a pre-existing eroded topography characterised by a high amplitude reflector (Fig. 8). This implies that, in this case, the backscatter is not sensitive to the nature of the surficial deposit but rather to the thickness of the deposit as well as the nature of the underlying unit. The high backscatter signal is not restricted to the channelled areas within zone 2, suggesting that turbidity current activity is not the primary factor here for a stronger signal. Indeed, the 3.5 kHz data show a perfect lateral continuity between the zones defined from the backscatter data (Figs. 3, 8). No overlaps or unconformities are observed laterally except where the network of channels is observed, suggesting that the entire area of chaotic topography may consist of a single synchronous retrogressive slump.

5.4. Creep, translational slide and debris flow in the southwest

Evidence for recent creep features and soft sediment deformation are found in the southwestern part of the studied area although the

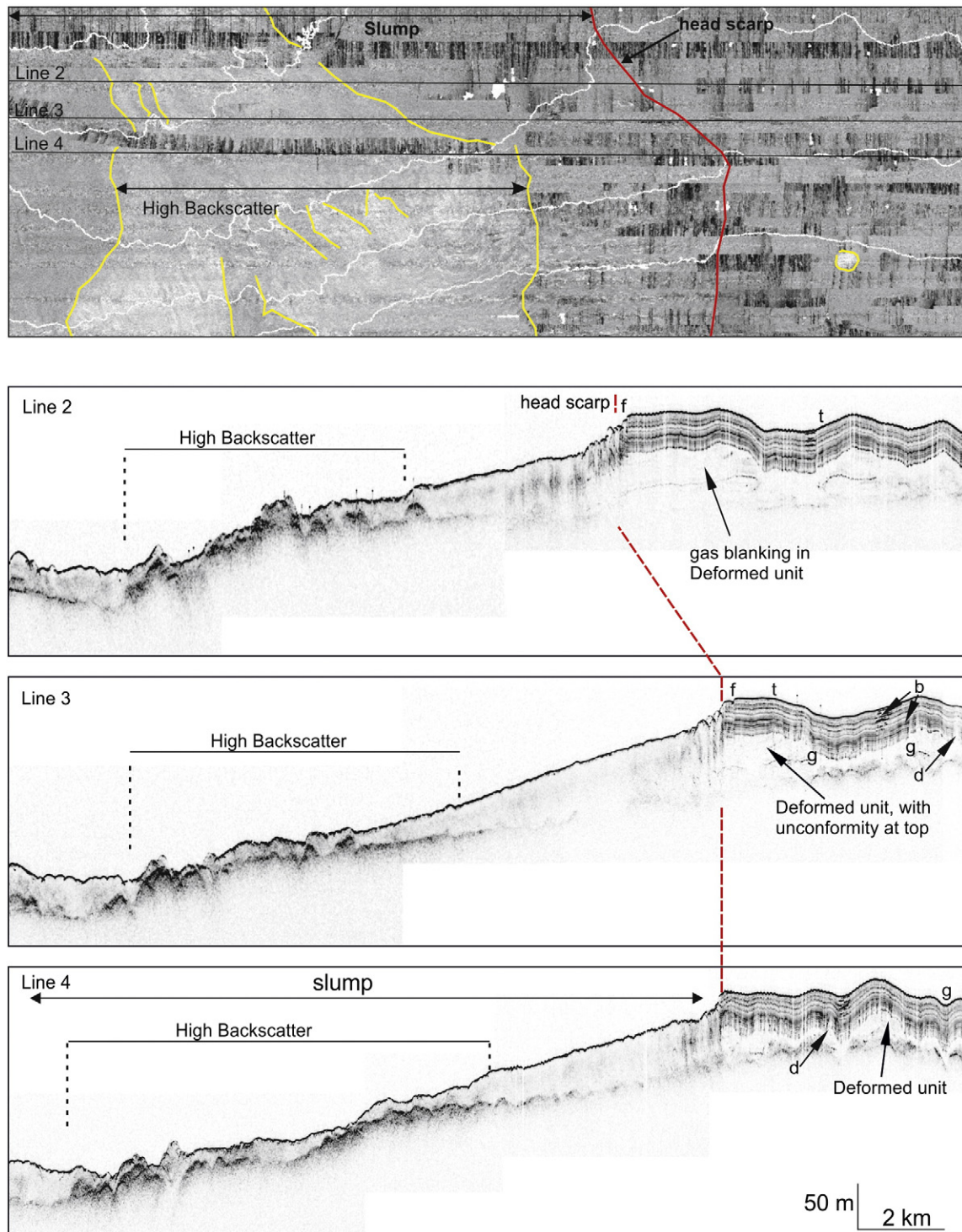


Fig. 8. Cross sections on the Ikit Delta slope showing style of deformation in the zone of creep as well as lateral changes in the multibeam backscatter signal compared to that from the 3.5 kHz. b = bright spot; d = diaper; f = fault at edge of slump; g = growth fault; t = tension crack. Note that the backscatter signal strength increases as the slump laterally thins out.

timing of these events appears different from the main Ikit slump. Apparent MTDs in the southwest area show generally smooth morphology and consist principally of transparent facies T1. The smooth morphology might be enhanced by a thin (~1 m) drape of hemipelagic sediment, not resolved by the sounder, overlying MTDs. Nevertheless, the T1 facies is acoustically more transparent than the chaotic facies (compare Fig. 6 with Fig. 7) and there is no trace of convex-downslope rotational slump ridges. Rather, the T1 facies appears to pass laterally into the S2 facies (Fig. 7b) or abruptly into the S1 facies (Fig. 7c), suggesting

that T1 represents comminuted stratified facies sediment in which any blocks have been destroyed to produce scattering rather than hyperbolic diffractions. There are no stratified remnants for the passage of gas through the MTD to concentrate below and produce bright spots (Fig. 7b).

MTD unit (2) consists of a tongue of facies S2, terminating downslope in convex-downslope parallel ridges (PR in Figs. 2, 7) and represents a style of deformation in which stratified sediment has deformed in large blocks, probably by creep, although acoustic

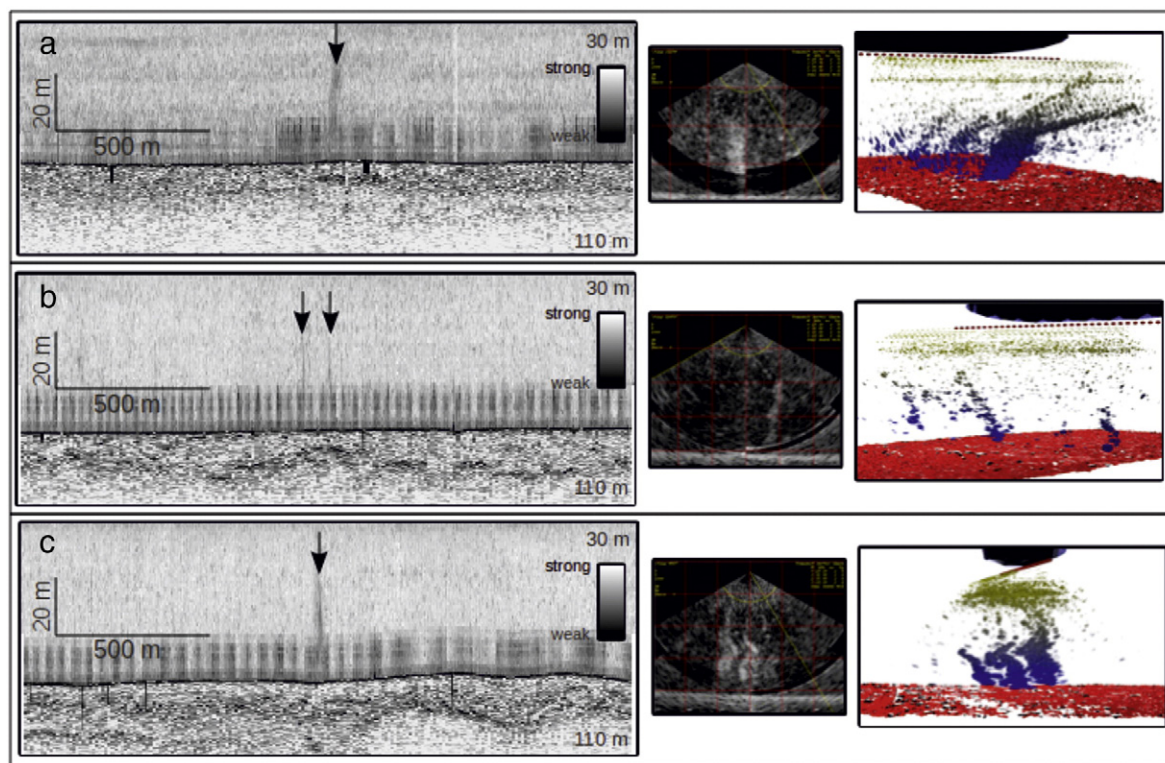


Fig. 9. Examples of vents found at clusters A, B, and C (see Fig. 4 for location map). Left: Composite of EM302 multibeam water column backscatter and 3.5 kHz sub-bottom. Water column data ~15 m at each side from nadir from each swath are collapsed into the profile. Backscatter levels are relative and cannot be compared between both data sets. Dark alternating slices near the seabed are interference of the previously transmitted swath when operating in dual-swath mode. Arrows indicating plume. Middle: Across-track profile of the plume. Right: 3D visualization of multibeam water column data showing the ship's hull, plume (blue–green scatters), and seabed (red scatters).

resolution is insufficient to unequivocally recognise growth faults. The decollement surface appears to be about 50 m subbottom (Fig. 7c) and translation on this surface has produced the compressive ridges (PR in Figs. 2, 7) at the distal end of the slide.

The larger MTD of facies T1 to the east of this translational slide, comprising units (2), (3) and (4) (Fig. 7), is underlain by stratified sediment and has a shallower decollement surface. It appears to represent complete comminution, perhaps by liquefaction, of the original muddy stratified facies. It flowed as one or more cohesive debris flows, producing a distinct snout and compressive ridge between profiles b and c downslope from unit (2) (Fig. 2). Unit (4) has marginal slopes of 2.5°–3° (Fig. 7c). The style of failure may have been initiated as a spread on the steep upper slope that previously underwent creep. Upslope of both the translational slide and the debris flow are numerous active gas plumes of cluster D (Fig. 4).

5.5. Role of thickness of the failure

Mid- to Late Holocene sediment on the Beaufort Slope consists of soft muds, whereas late Pleistocene glaciomarine clays are more consolidated and presumably become increasingly consolidated with increasing sub-bottom depth. In the south-western area, failures in the upper 25 m of the section appear to have transformed into acoustically transparent debris flow (units (2) and (4) in Fig. 7), whereas failures on a decollement surface 40–50 m subbottom have only deformed by creep (Fig. 7c, eastern part).

An analogous contrast between shallow soft sediment and deeper more consolidated sediment is interpreted for the retrogressive Ikit slump in the central area (Fig. 6). The chaotic echofacies corresponds to back-tilted blocks, presumably of well consolidated sediment. The transparent echofacies downslope appears analogous to the muddy

debris flow deposits in the south-western area (Fig. 7) and may have formed in a similar manner from surficial, little consolidated silty muds. It overlies buried chaotic facies, implying a source from the upper slope.

Downslope in the Ikit slump, 2 km seaward of an increase in gradient from 1.7° to 2.9°, the subparallel blocks are no longer visible (Fig. 6) and the last blocks appear to overlie a reflective subplanar surface. This is interpreted as marking the basal shear plane of the rotational slump or the decollement surface for a spread, which has been completely evacuated of failed material on the steeper slope, as demonstrated elsewhere (Piper et al., 1985, 1999). Muddy debris flow deposits created from disintegration of the upper part of slump blocks has then covered the evacuation surface.

5.6. Roles of permafrost and shallow gas

Relationships between landslides and gas-rich sediment related to dissociation of gas hydrates have been previously suggested to explain some past large scale submarine failures (Jung and Vogt, 2004; Sultan et al., 2004; Faure et al., 2006), including the well-known Storegga Slide (Canals et al., 2004; Sultan et al., 2004; Paull et al., 2007). Nevertheless, the lack of sediment preservation after the Storegga failure and the absence of active gas vents do not allow a clear demonstration of the role of dissociation of gas hydrates.

In our case, the abundance and distribution of the gas plumes, in association with the failure headscarps, and of creep and debris flows all along the northern edge of subsea permafrost suggest a significant interconnection among the different features and gas. Past work on Beaufort Sea subsea permafrost suggested upwardly migrating gas from depth and within the thick permafrost, which then escapes at the northern edge of the permafrost along the shelf edge as evidenced

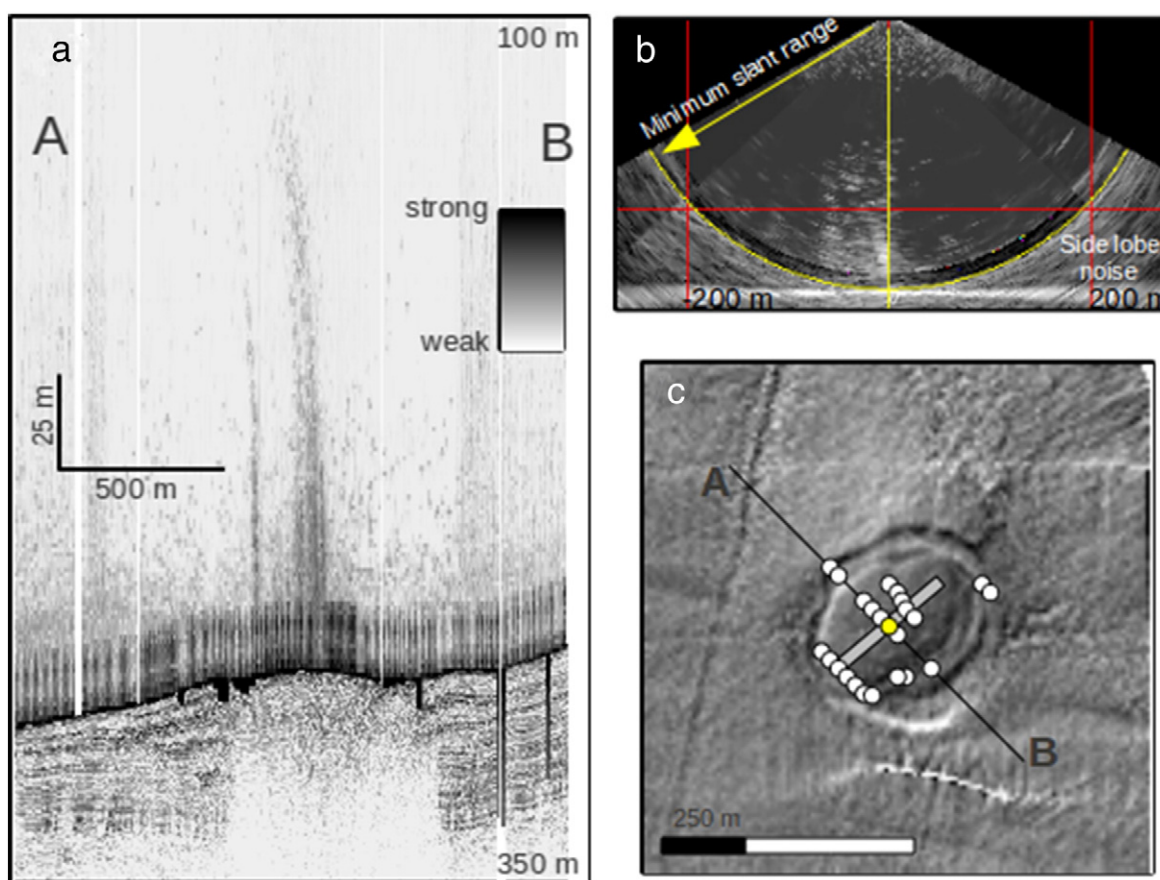


Fig. 10. (a) Composite of EM302 multibeam water column backscatter and 3.5 kHz sub-bottom. Plume venting from top of the mud volcano clearly stands out among background noise seen left and right of the mud volcano. (b) An across-track profile of a plume (yellow dot in Fig. 9c). (c) Hill shaded image of the mud volcano with locations of: plumes detected from several passes (dots), composite profile (line A → B), and the across-track profile (grey rectangle). See Fig. 2 for location.

by the linear distribution of several hundred mud volcanoes (Blasco et al., 2013). Decomposing gas hydrates under the Beaufort Shelf predicted by Paull et al. (2012) may have contributed to the quantity of migrating gas and associated water. Upward migration of gas and water is likely episodic, due to breaching and resealing of permeability barriers (Mourgues et al., 2012). The migrating gas and associated water (Fig. 11) are trapped in porous sediments that are capped by the 30 m thick silty clay. As more gas and water are trapped, the strength of the sediment decreases and the gas-rich layer starts to spread under the weight of the overlying unit, spreading that eventually lead to the failure when the pore pressure exceeds the sediment plasticity. In addition, enhanced gas release may trigger failures, as proposed by Panieri et al. (2012) and abundant gas in sediments may be a preconditioning factor for failure triggered by earthquakes, which could also be the cause of the widespread apparently synchronous retrogressive Ikit slump. Shallow gas plays a demonstrable role in widespread creep deformation, which in places has evolved into translational slides and comminuted debris flows.

Adjacent to the eastern edge of the study area, where the upper slope has not failed, are several hundred PLFs. The trend of mud volcanoes may have continued west along the shelf break in the study area but was consumed by the slope failures described here. Water column gas plumes have the greatest density at the headscarp where the trend of PLFs would have existed. In addition, the linear southern edge of the slope failures (Fig. 2) is probably controlled by the northern edge of the ice-bearing permafrost. This model implies that shelf break and upper slope stability in the Canadian Beaufort Sea are strongly linked to the dynamics of subsea permafrost and associated migration of significant quantities of gas.

6. Conclusions

- Four styles of shallow slope deformation are recognised on the central Beaufort Slope:
 - Failures initiated on steep channel walls in deep water have retrogressed to the shelf edge in the last 1000 years to form the Ikit slump. Upslope, they consist of concave-downslope blocks on gradients of $<2^\circ$, which pass downslope into debris flows that proximally overlie blocks. On the 3° mid slope, blocks were completely evacuated and debris flow deposits overlie the basal slide surface. Backscatter intensity depends on the thickness of the debris flow.
 - Creep is widespread on the outer shelf and upper slope, in a unit 25–50 m thick overlying a gas-charged deformed decollement unit. Creep has occurred progressively throughout the Holocene, based on the record of growth faults.
 - On slopes $>3^\circ$, thick (50 m) units that creep may evolve into a translational slide with toe thrusts.
 - On slopes $>3^\circ$, thinner creep units (<25 m) may evolve into dispersed muddy debris flows with run-out of <10 km. Likewise, muddy debris flows appear to evolve from the upper parts of rotational or spreading slump blocks and cover the distal parts of the retrogressive Ikit slump.
- Active gas venting is concentrated near the present limit of subsea permafrost. Gas charged sediment in the deformed decollement zones in places reaches the seabed as mud volcanoes. The role played by gas is difficult to quantify, but creep and subsequent failure features are much more common than on most upper continental slopes where gas is less abundant.

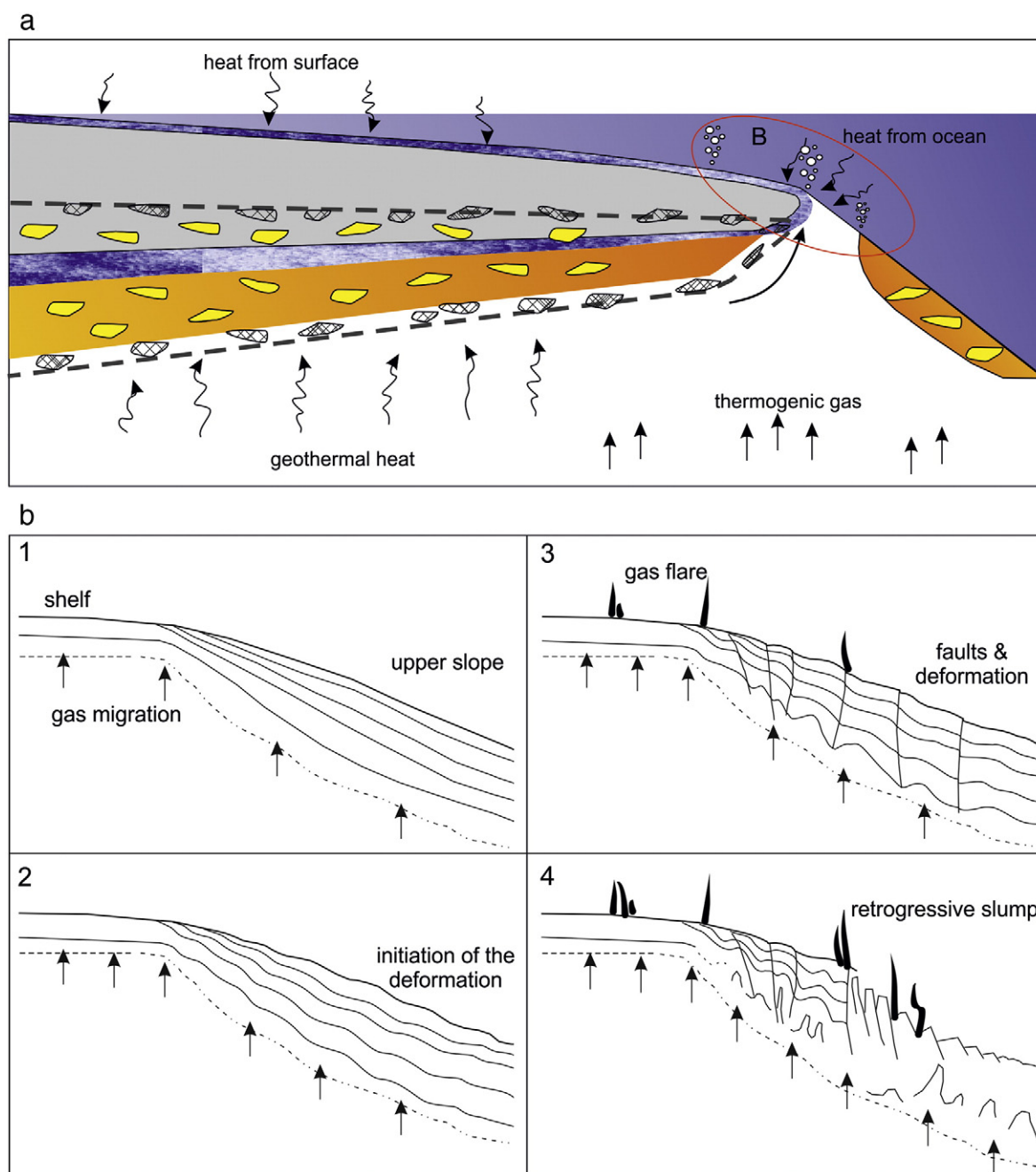


Fig. 11. (A) Schematic cross section of the current state of the Beaufort Shelf and slope outlining subsurface zones where permafrost (blue) and gas hydrate (cross hatch) have decomposed (adapted from Paull et al., 2012 and Blasco et al., 2013). (B) Schematic model of progressive post-glacial to Holocene deformation and failure.

Acknowledgements

The authors would like to thank Robbie Bennett for providing critical discussion during the compilation of this publication. An early draft of the manuscript was significantly improved based on internal review of Philip Hill, and further improved after journal reviews by Joshu Mountjoy and an anonymous reviewer. Data were collected on cruise 2009-11 of the Canadian Coast Guard icebreaker Amundsen: we thank the ship's company for their support. Multibeam bathymetry data were collected by the Ocean Mapping Group at the University of New Brunswick through the ArcticNet programme. This study was supported by funding from the Geological Survey of Canada and from a Natural Sciences and Engineering Research Council of Canada Discovery Grant to DJWP.

References

- Atkinson, G.M., Charlwood, R.G., 1988. Seismic hazard maps for northern and western Canadian offshore regions. Canada Oil and Gas Lands Administration Special Publication. Natural Resources Canada, Ottawa (March 1988).
- Best, A.I., Clayton, C.R.I., Longva, O., Szuman, M., 2003. The role of free gas in the activation of submarine slides in Finnøidjorden. In: Locat, J., Mienert, J. (Eds.), *Submarine Mass Movements and Their Consequences*. Kluwer Acad. Publ, Dordrecht, The Netherlands, pp. 491–498.
- Blasco, S., Woodworth-Lynas, C., Rankin, S., Hawkins, J., Dingle, J., 2012. Outer shelf and upper slope seabed dynamics. Canadian Beaufort Sea based on Geological Data. ArcticNet Annual Science Meeting, December 10–13 (Vancouver, B.C. Program with Abstract <http://www.arcticnetmeetings.ca/asm2012/index.php>).
- Blasco, S., Bennett, R., Brent, T., Burton, M., Campbell, P., Carr, E., Covill, R., Dallimore, S., Davies, E., Hughes-Clarke, J., Issler, D., MacKillop, K., Mazzotti, S., Patton, E., Shearer, J., White, M., 2013. 2010 state of knowledge: Beaufort Sea seabed geohazards associated with offshore hydrocarbon development. Geological Survey of Canada Open File 6989 (307 pp.).

- Bringué, M., Rochon, A., 2012. Late Holocene paleoceanography and climate variability over the Mackenzie Slope (Beaufort Sea, Canadian Arctic). *Marine Geology* 291–294, 83–96.
- Canals, M., Lastras, G., Urgeles, R., Casamor, J.L., Mienert, J., Cattaneo, A., De Batist, M., Haflidason, H., Imbo, Y., Laberg, J.S., Locat, J., Long, D., Longva, O., Masson, D.G., Sultan, N., Trincardi, F., Bryn, P., 2004. Slope failure dynamics and impacts from seafloor and shallow sub-seafloor geophysical data: case studies from the COSTA project. *Marine Geology* 213, 9–72.
- Carson, M.A., Jasper, J.N., Conly, F.M., 1998. Magnitude and sources of sediment input to the Mackenzie Delta, Northwest Territories, 1974–94. *Arctic* 51 (2), 116–124.
- Casas, D., Ercilla, G., Baraza, J., 2003. Acoustic evidence of gas in the continental slope sediments of the Gulf of Cadiz (E Atlantic). *Geo-Marine Letters* 23, 300–310.
- Cassidy, J.F., Rogers, G.C., Lamontagne, M., Halchuk, S., Adams, J., 2010. Canada's earthquakes: 'the good, the bad, and the ugly'. *Geoscience Canada* 37, 1–16.
- Correggiari, A., Trincardi, F., Langone, L., Roveri, M., 2001. Styles of failure in late Holocene highstand and prodelta wedges on the Adriatic shelf. *Journal of Sedimentary Research* 71 (2), 218–236.
- Faure, K., Greinert, J., Pecher, I.A., Graham, I.J., Massoth, G.J., de Ronde, C.E.J., Wright, I.C., Baker, E.T., Olson, E.J., 2006. Methane seepage and its relation to slumping and gas hydrate at the Hikurangi margin, New Zealand. *New Zealand Journal of Geology and Geophysics* 49, 503–516.
- Hill, P.R., Moran, K., Blasco, S., 1982. Creep deformation of slope sediments in the Canadian Beaufort Sea. *Geo-Marine Letters* 2, 163–170.
- Hill, P.R., Mudie, P.J., Moran, K., Blasco, S.M., 1985. A sea-level curve for the Canadian Beaufort Shelf. *Canadian Journal of Earth Sciences* 22, 1383–1393.
- Hill, J.C., Driscoll, N.W., Weissel, J.K., Goff, J.A., 2004. Large-scale elongated gas blowouts along the U.S. Atlantic margin. *Journal of Geophysical Research* 109, B09101. <http://dx.doi.org/10.1029/2004JB002969>.
- Hughes Clarke, J.E., 2006. Applications of multibeam water column imaging for hydrographic survey. *The Hydrographic Journal* 120, 3–14.
- Hughes Clarke, J.E., 2012. SwathEd. Unix/linux. Fredericton: Ocean Mapping Group. University of New Brunswick.
- Hughes Clarke, J.E., Iwanowska, K.K., Parrott, R., Duffy, G., Lamplugh, M., Griffin, J., 2008. Inter-calibrating multi-source, multi-platform backscatter data sets to assist in compiling regional sediment type maps: Bay of Fundy, Paper 8-2. *Proceedings of the Canadian Hydrographic Conference and National Surveyors Conference*, Victoria, BC, p. 22.
- Hughes Clarke, J.E., Brucker, S., Muggah, J., Church, I., Cartwright, D., Kuus, P., Hamilton, T., Pratomo, D., Eisan, B., 2012. The Squamish ProDelta: monitoring active landslides and turbidity currents. *Canadian Hydrographic Conference* 2012, p. 15.
- Jung, W.-Y., Vogt, P.R., 2004. Effects of bottom water warming and sea level rise on Holocene hydrate dissociation and mass wasting along the Norwegian–Barents Continental Margin. *Journal of Geophysical Research* 109, B06104.
- Kvenvolden, K.A., 1999. Potential effects of gas hydrate on human welfare. *Proceedings of the National Academy of Sciences* 96, 3420–3426.
- Lamontagne, M., Halchuk, S., Cassidy, J.F., Rogers, G.C., 2008. Significant Canadian earthquakes of the period 1600–2006. *Seismological Research Letters* 79, 211–223.
- Lee, H.J., Syvitski, J.P., Parker, G., Orange, D., Locat, J., Hutton, E.W., Imran, J., 2002. Distinguishing sediment waves from slope failure deposits: field examples, including the 'Humboldt slide', and modelling results. *Marine Geology* 192 (1), 79–104.
- Li, X., He, S., 2012. Progress in stability analysis of submarine slopes considering dissociation of gas hydrates. *Environmental Earth Sciences* 66, 741–747.
- Maslin, M., Owen, M., Betts, R., Day, S., Dunkley, Jones T., Ridgwell, A., 2010. Gas hydrates: past and future geohazard? *Philosophical Transactions of the Royal Society A: Mathematical, Physical and Engineering Sciences* 368, 2369–2393.
- Micallef, A., Masson, D.G., Berndt, C., Stow, D.A.V., 2007. Morphology and mechanics of submarine spreading: a case study from the Storegga Slide. *Journal of Geophysical Research* 112, F03023.
- Mosher, D.C., Moscardelli, L., Shipp, R., et al., 2010. Submarine mass movements and their consequences: introduction. In: Mosher, D.C., Shipp, C., Moscardelli, L., Chaytor, J., Baxter, C., Lee, H., Urgeles, R. (Eds.), *Submarine Mass Movements and Their Consequences: IV. Advances in Natural and Technological Hazards Research*, 28. Springer, Dordrecht, Netherlands, pp. 1–8. <http://dx.doi.org/10.1007/978-90-481-3>.
- Mourgues, R., Bureau, D., Bodet, L., Gay, A., Gressier, J.B., 2012. Earth and Planetary Science Letters 313, 67–78.
- Mulder, T., Cochonat, P., 1996. Classification of offshore mass movements. *Journal of Sedimentary Research* 66, 43–57.
- Nixon, M.F., Grozic, J.L., 2007. Submarine slope failure due to gas hydrate dissociation: a preliminary quantification. *Canadian Geotechnical Journal* 44, 314–325.
- Panieri, G., Camerlenghi, A., Cacho, I., Cervera, C.S., Canals, M., Lafuerza, S., Herrera, G., 2012. Tracing seafloor methane emissions with benthic foraminifera: results from the Ana submarine landslide (Eivissa Channel, Western Mediterranean Sea). *Marine Geology* 291–294, 97–112.
- Paull, C.K., Ussler III, W., Holbrook, W.S., 2007. Assessing methane release from the colossal Storegga submarine landslide. *Geophysical Research Letter* 34, L04601.
- Paull, C., Dallimore, S., Hughes-Clarke, J., Blasco, S., Lundsten, E., Ussler III, W., Graves, D., Sherman, A., Conway, K., Melling, H., Vagle, S., Collett, T., 2012. Tracking the decomposition of permafrost and gas hydrate under the shelf and slope of the Beaufort Sea. 7th International Conference on Gas Hydrate, Edinburgh, p. 12.
- Piper, D.J.W., Farre, J.A., Shor, A., 1985. Late Quaternary slumps and debris flows on the Scotian Slope. *Geological Society of America Bulletin* 96 (12), 1508–1517.
- Piper, D.J.W., Cochonat, P., Morrison, M.L., 1999. Sidescan sonar evidence for progressive evolution of submarine failure into a turbidity current: the 1929 Grand Banks event. *Sedimentology* 46, 79–97.
- Rogers, K.G., Goodbred, S.L., 2010. Mass failures associated with the passage of a large tropical cyclone over the Swath of No Ground submarine canyon (Bay of Bengal). *Geology* 38, 1051–1054.
- Schell, T.M., Scott, D.B., Rochon, A., Blasco, S., 2008. Late Quaternary paleoceanography and paleo-sea ice conditions in the Mackenzie Trough and Canyon, Beaufort Sea. *Canadian Journal of Earth Sciences* 45 (11), 1399–1415.
- Schneider von Deimling, J., Brockhoff, J., Greinert, J., 2007. Flare imaging with multibeam systems: data processing for bubble detection at seeps. *Geochemistry, Geophysics, Geosystems* 8, Q06004. <http://dx.doi.org/10.1029/2007GC001577>.
- Scott, D.B., Schell, T., St-Onge, G., Rochon, A., Blasco, S., 2009. Foraminiferal assemblage changes over the last 15,000 years on the Mackenzie–Beaufort Sea Slope and Amundsen Gulf, Canada: Implications for past sea ice conditions. *Paleoceanography* 24, PA2219. <http://dx.doi.org/10.1029/2007PA001575>.
- Shearer, J., MacNab, R., Pelletier, B., Smith, T., 1971. Submarine pingos in the Beaufort Sea. *Science* 174, 816–818.
- Shillington, D.J., Seeber, L., Sorlien, C.C., Steckler, M.S., Kurt, H., Dondurur, D., Çifçi, G., Imren, C., Cormier, M.-H., McHugh, C.M.G., Gürçay, S., Poyraz, D., Okay, S., Atgin, O., Diebold, J.B., 2012. Evidence for widespread creep on the flanks of the Sea of Marmara transform basin from marine geophysical data. *Geology* 40 (5), 439–442.
- Sultan, N., Cochonat, P., Foucher, J.P., Mienert, J., 2004. Effect of gas hydrates melting on seafloor slope instability. *Marine Geology* 213, 379–401.
- Syvitski, J.P.M., Burrell, D.C., Skei, J.M., 1987. *Fjords: Processes and Products*. Springer-Verlag.
- Urgeles, R., Cattaneo, A., Puig, P., Lique, C., De Mol, B., Amblàs, D., Trincardi, F., 2011. A review of undulated sediment features on Mediterranean prodeltas: distinguishing sediment transport structures from sediment deformation. *Marine Geophysical Research* 32 (1–2), 49–69.
- Vilks, G., Wagner, F.J.E., Pelletier, B.R., 1979. The Holocene marine environment of the Beaufort Shelf. *Geological Survey of Canada Bulletin* 303, 43.